Rare earth doping of topological insulators: A brief review of thin film and heterostructure systems

T. Hesjedal[1,*]

[1] Department of Physics, Clarendon Laboratory, University of Oxford, Oxford, OX1 3PU, United Kingdom

Received XXXX, revised XXXX, accepted XXXX
Published online XXXX

Key words: topological insulators, rare earth doping, bismuth telluride, antimony telluride, heterostructure, MBE

* Corresponding author: e-mail thorsten.hesjedal@physics.ox.ac.uk, Phone: +44-1865-272235, Fax: +44-1865-282208

Magnetic topological insulators (MTIs) are a novel materials class in which a topologically nontrivial electronic band structure coexists with long-range ferromagnetic order. The ferromagnetic ground state can break time-reversal symmetry, opening a gap in the topological surface states whose size is dependent on the magnitude of the magnetic moment. Doping with rare earth ions is one way to introduce higher magnetic moments into a material, however, in Bi_2Te_3 bulk crystals, the solubility limit is only a few percent. Using molecular beam epitaxy for the growth of doped $(Sb,Bi)_2(Se,Te)_3$ TI thin films, high doping concentrations can be achieved while preserving their high crystalline quality. The growth, structural, electronic, and magnetic properties of Dy, Ho, and Gd doped TI thin films will be reviewed. Indeed, high magnetic moments can be introduced into the TIs, which are, however, not ferromagnetically ordered. By making use of interfacial effects, magnetic long-range order in Dy doped Bi_2Te_3, proximity-coupled to the MTI Cr:Sb_2Te_3, has been achieved. Clearly, engineered MTI heterostructures offer new possibilities that combine the advantageous properties of different layers, and thus provide an ideal materials platform enabling the observation new quantum effects at higher temperatures.

1 Introduction Topological insulators (TIs) feature among the most significant contemporary discoveries in condensed matter physics [1–3]. They have a gapless topological surface state (TSS) which exhibits robust spin-momentum locking protected by time-reversal symmetry (TRS) from backscattering by non-magnetic defects. The observation of novel physical phenomena in TIs, e.g., Majorana fermions [4], the quantum anomalous Hall effect (QAHE) [5] and topological magneto-electric effects [6], as well as low-power electronic and spintronic device applications [7], contribute to the popularity of TIs.

In magnetic topological insulators (MTIs), the topologically nontrivial electronic band structure coexists with long-range ferromagnetic order. The ferromagnetic ground state can break TRS, introducing a gap in the Dirac-cone-shaped TSS around the Dirac point [8], which is the prerequisite for realizing the QAHE [9]. Long-range ferromagnetically ordered MTIs can be achieved by doping the TI with transition metals. Examples are Fe [10] and Mn [11–13] doped Bi_2Te_3, and V doped Sb_2Te_3 [14] bulk crystals. Apart from introducing magnetic order, the dopants should not introduce excess scattering centers and additional bulk carriers, which would be detrimental for the observation of the QAHE in MTIs. Cr doped $(Bi_{0.1}Sb_{0.9})_2Te_3$ has been the most successful QAHE system so far with a Curie temperature of $T_C \approx 16$ K [5,15,16]. Despite the fact that these Cr doped films can have magnetic ordering temperatures above 100 K without loss of crystalline quality [17], the observation of the QAHE has been restricted to very low temperatures (<300 mK) [5,16], which has been ascribed to extreme Dirac-mass disorder [18]. Further, despite being well-behaved from a growth perspective, substitutional Cr doping into this materials class (replacing Bi^{3+}), was found to lead to nominally divalent Cr and covalent bonding, thereby altering the structural and magnetic properties [19,20].

In an attempt to increase the useful QAHE temperature range, a number of more unconventional doping approaches have been successfully explored, such as co-doping [21–23], modulation doping to separate the dopant from the charge-carrying surface state layer [24,25], and doping with higher magnetic moment rare earth ions [26, 27], to name a few. Note that co-doping with different transition metals can also lead to undesired phase separations in this materials class [28], while modulation doping with Cr promises greater inherent benefits owing to the nature of the doping mechanism, which have, e.g., led to the first successful observation of the axion insulator state [29]. Modulation doping of heterostructures, i.e., non-uniform doping along the growth direction, is a well-known technique for achieving ultrahigh electron mobilities in III-V semiconductors [30]. Fundamentally, it is based on the spatial separation of the location of the donors, which have the detrimental effect of acting as scatterers, and the carriers they introduce [31]. Analogously, modulation doping with ions that introduce long-range magnetic order, and thus open a magnetic gap, can reduce their detrimental effect on the carriers in the topological surface state.

Doping a TI with an ion that has a higher magnetic moment is an interesting alternative approach, in particular since the size of the magnetic gap is directly dependent on the size of the magnetic moment [32]. The rare earth elements comprise of the lanthanide series ($4f$ series) and the more exotic actinide series ($5f$ series). The lanthanides (Ln), reaching from La to Yb, are well-established in the context of thin film growth. The magnetic moments (m_{eff}) peak in the Ln series for Dy and Ho with values of $\sim$10.5 μ_{B}. Other large moment ions are the lighter Gd and Tb, as well as the heavier Er and Tm. In general, due to their well-shielded $4f$ shell, the expectation is that the high moment Ln ions behave like isolated magnetic moments in the host matrix, thereby giving rise to an overall paramagnetic behavior of the doped system. Also in Ln metals, the conduction electrons contribute to the magnetic properties primarily as a means of exchange coupling between the localized $4f$ moments. Nevertheless, this view of non-hybridizing Ln states is a simplification and the existence of correlated (atomic-like) $4f$ electrons in the vicinity of the valence band makes any first-principles theory challenging [33]. Evidence for $4f$ delocalization and dispersion was found in, e.g., in $CeSb_2$ [34], $CeCoGe_{1.2}Si_{0.8}$ [35], $YbRh_2Si_2$ [36], and also Gd doped HfO_2 where strong hybridization with the O $2p$ band was demonstrated [37]. Density-functional theory for rare earth elements can now also include the important contributions of spin-orbit interaction and orbital polarization, which determine the magnitude of the magnetic moments [33]. Furthermore, for $LaBiTe_3$ (with a 1:1 ratio of La:Bi) [38] and $Gd_{0.08}Bi_{1.92}Se_3$ [39], *ab initio* calculations of the band structure have shown that these materials remain TIs upon RE doping. Finally, owing to their noncentrosymmetric crystal structure, compounds such as $LaBi_{1-x}Sb_xTe_3$ (with x between 38.5% and 41.9%) further exhibit a Weyl semimetal phase [40]. In conclusion, owing to complexity of predicting their magnetic properties, only the growth and characterization of rare earth (RE) doped materials will be able to answer the question whether both long-range ferromagnetic order and low bulk carrier concentrations can be achieved while maintaining the topologically non-trivial surface states.

Doping with Gd is an obvious choice as it is easy to handle from a practical standpoint [41,42]. In the Gd metal, both the $5d$ and $6s$ electrons are lost to the conduction band, leaving a highly localized magnetic moment due to the unpaired electrons in the $4f$ shell behind. The f shell is half-filled and the (Hund's rule) ground state is $^8S_{7/2}$ without spin-orbit splitting. The large magnetic moment arises from the 7 unpaired $4f$ spins. The $4f$ are well-shielded by the filled $5s$ and $5p$ shells and do therefore only play a minor role in the chemical and mechanical properties of Gd, however, determine the magnetic properties. In the metal, the conduction electrons contribute to the magnetic properties primarily as a means of exchange coupling between the localized $4f$ moments. The crystal field is completely shielded by the complete $5s$ and $5p$ shells, therefore the orbital moment of the $4f$ electrons is not quenched and the total angular momentum is essentially that of the free ion. In the metal, the large total moment is strongly interacting with the weak crystalline field, resulting in large anisotropies of the magnetic properties. Dysprosium metal has a magnetic ordering temperature of $T_{\mathrm{Neel}} = 178.5$ K [43]. Below this temperature, it shows ferromagnetic ordering in the basal plane, whereby the magnetic moment rotates in subsequent basal planes giving rise to a spin spiral [44]. Below the Curie temperature of 85 K, Dy becomes ferromagnetically ordered throughout [45].

Unfortunately, Gd doped Bi_2Te_3 bulk crystals [41,42] were plagued by the low solubility limit of $\sim$1% and 5%. Therefore, thin films were explored which allow for the growth of thermodynamically unstable materials, and thus in principle also higher doping concentrations. For Gd doped materials, Harrison *et al.* found a solubility limit of $\sim$30% in Bi_2Te_3 [46], which started the exploration of a wider range of RE dopants and their physical properties. This review summarizes the developments in RE doping of single-crystalline $(Bi,Sb)_2(Se,Te)_3$ thin film TIs over the past years. The focus will be on the most promising candidate, Dy doped Bi_2Te_3, in which a gapped topological surface state band has been observed despite the absence of long-range magnetic order [27]. Finally, by combining high ordering temperature, Cr doped Sb_2Te_3 thin films with Dy doped Bi_2Te_3 in high quality heterostructures, ferromagnetic ordering up to 17 K has been induced in the Dy doped layer. This demonstrates that through engineering of the heterostructure, the high moment of the rare earth can have long-range magnetic order through the proximity to a Cr doped TI layer, which concludes this review.

2 Growth and structural properties of RE doped $(Bi,Sb)_2(Se,Te)_3$ thin films $(Bi,Sb)_2(Se,Te)_3$ compounds have a rhombohedral crystal structure with space group D^5_{3d} ($R\bar{3}m$). Figure 1 illustrates the layered structure of the unit cell, with five atomic layers (Te–Bi–Te–Bi–Te in this example) forming a quintuple layer (QL). Adjacent Te layers are weakly bonded across the van der Waals gap. Several studies have reported the growth of high-quality, single crystalline thin films by molecular beam epitaxy (MBE) on single-crystalline substrates, e.g., Si [47–50], Al_2O_3 [51,52], GaAs [53–55], and lattice-matched InP [56,57] to name a few, as well as amorphous SiO_2/Si for back-gated electrical transport measurements [58–61].

Rare-earth doped $(RE_xBi_{1-x})_2Te_3$ thin films with varying RE doping concentration x were grown by MBE on c-plane sapphire as described in detail for Dy [26,27], Ho [62], and Gd [46,63]. The three-chamber MBE system used for most of the study has a base pressure of 1×10^{-10} Torr and is equipped with standard effusion cells for the evaporation of Dy, Ho, Bi, and Te. A high temperature effusion cell was used for Gd in another system. The elemental materials were of the highest purity available, i.e., 99.9999% for Bi and Te, 99.99% for Dy and Ho and 99.9% for Gd. Following the established two-step recipe for Bi_2Te_3 [51], first a seed layer was deposited at 50°C lower than the growth temperature used for the remainder of the film. The growth was carried out with a Te:Bi overpressure of >10:1, as measured with a beam flux monitor. The growth rate is limited by the incident Bi flux and varies as a function of substrate temperature. Next, the films were annealed under Te flux for 30 min, while the temperature was ramped up to the final growth temperature of 300°C for Dy and Ho and 240°C for Gd (all temperatures are thermocouple values). Note that the Gd doped films were grown in a different MBE system, using a different sample heater assembly. The film thicknesses were typically between 50 and 120 nm, and were grown at a rate of typically ∼0.5 nm/min. For achieving doping concentrations as listed in Table 1, effusion cell temperatures of 825-950°C for Dy, 840-900°C for Ho, and 1250-1400°C for Gd were used.

The stoichiometry of the films, as well as their thicknesses, were determined by using Rutherford backscattering spectrometry (RBS) with 2.3 MeV helium ions, in combination with particle induced x-ray emission (PIXE) with 1 MeV hydrogen ions. Note that the reliable *in-situ* flux measurement using a beam flux monitoring is not possible for REs due to gettering effects. The ratio of the combined Bi and RE cation to anion fraction was determined to be ∼2:3, consistent with a substitutional doping scenario with the RE^{3+} ion isoelectronically substituting for Bi^{3+}. Note that all films show small amounts of unintentional Se doping as the growth was carried out in a combined selenide and telluride MBE. As Se is replacing Te in the TI films, the combined chalcogen atomic percentages are ∼60%.

The morphology of the growing films was monitored *in-situ* using reflection high-energy electron diffraction (RHEED). Figure 2 shows the typical streaky RHEED patterns, indicative of flat, crystalline surfaces, for the Dy doping series up to $x = 0.355$. For doping concentrations greater than 0.183, the streaks become more diffuse as the surface becomes rougher. Streak-like RHEED patterns were observed for all high-quality samples of the RE doping series, i.e., for lower doping concentrations [26,46, 62].

The film morphology was investigated using atomic force microscopy (AFM) and scanning electron microscopy (SEM). Figure 3(a) shows that the morphology of the undoped film (AFM image) is dominated by triangular terraces. The terraces typically show 1-nm-high quintuple layer steps. With increasing doping level going from $x = 0.055$ (b), to 0.113 (c), and 0.355 (d) (all SEM images), the density of triangular structures increases. This means that doping increases the number of seeds during growth. For a more detailed analysis of the morphology of the Dy doped films as a function of doping concentration, we refer to Ref. [26].

A detailed analysis of the structural properties of the films was carried out using x-ray diffraction (XRD) with Cu $K_{\alpha 1}$ radiation. Figure 4(a) compares an undoped Bi_2Te_3 film and a Dy doped film with $x = 0.355$. Across all doping series, only substrate and (0 0 3l) film peaks were observed, meaning that even for the high RE concentrations, the films remain c-axis oriented, rhombohedral single crystals. No secondary phases were observed at these lower doping concentrations. Peak broadening and intensity variations, indicative of degradation in crystalline quality, were observed with increasing doping concentration [26,63,64].

Also, as shown in Fig. 4(b), the peak positions shift towards lower diffraction angles, i.e., the c-axis lattice constant increases with increasing Dy concentration. The c-axis lattice constants vary from 30.39 Å for the undoped Bi_2Te_3 film to 30.83 Å for the $x = 0.355$ film. The in-plane lattice constants shown in Fig. 4(b) were obtained from asymmetric 2D reciprocal space mapping (not shown; details can be found in Ref. [26]). For comparison, the a- and c-axis lattice parameters for the rhombohedral $(Dy_xBi_{1-x})_2Te_3$ compound with $x = 0.5$ are a = 4.14 Å and c = 31.02 Å, respectively [65]. This means that the trend with doping concentration shown in Fig. 4(b) is consistent with a continuous substitutional doping scenario in the $(Dy_xBi_{1-x})_2Te_3$ series. Above (and including) $x = 0.355$, deviations in this trend are observed, pointing towards a departure from the substitutional doping scenario, and consistent with the different growth morphology observed in Fig. 3(d).

Figure 4(c) shows a comparison of XRD spectra of an undoped and selected Dy, Ho, and Gd doped films, which are very similar. Below a maximum RE doping concentration the thin films maintain the crystal structure of the un-

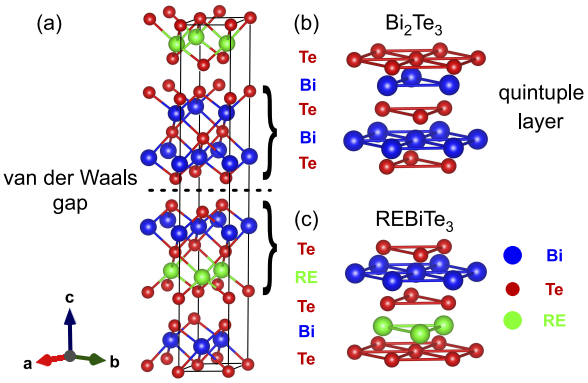

Figure 1 Undoped and rare earth (RE) doped Bi_2Te_3 crystal structure (Bi = blue, Te = red, RE = green). (a) Unit cell consisting of three Te-Bi-Te-Bi-Te quintuple layers (b), which are separated by the van der Waals gap between weakly bound Te layers. (c) RE doped Bi_2Te_3 quintuple layer. The REs are substitutionally replacing Bi. For simplicity, the dopants are shown in a single layer only. Note that apart from substitutional REs on Bi sites, the REs can also be incorporated interstitially, either in the van der Waals gap and within a quintuple layer. Figure reproduced from CC-BY 4.0 open access publication [27].

doped film, accompanied by small relative peak shifts and broadening of the rocking curves, and were free of secondary RE-Te or other phases. The critical concentrations, as a fraction of the Bi concentration in $(RE_xBi_{1-x})_2Te_3$, are 0.355 for Dy, 0.21 for Ho, and >0.30 for Gd. In contrast, for transition metal doped TI systems, phase segregation occurs at much lower doping concentrations than achieved for RE doped films [66].

To conclude the growth and basic structural analysis section, the growth parameters and c-axis lattice constants of the investigated thin film samples are summarized in Table 1. Independent of the RE dopant, the c-axis lattice constants of the films increase with doping concentration. The values for Gd and Ho doping are very similar, and smaller for Dy doping. These increases of the lattice constants are not directly correlated with the ionic radii, which are (for 3+ ions in octahedral coordination) 1.17 Å for Bi, 1.027 Å for Dy, 1.015 Å for Ho, and 1.053 Å for Gd.

To explore the structural properties of the Dy doped films in more detail, scanning transmission electron microscopy (STEM) was carried out (see Ref. [27] for details). Figure 5(a) shows a high-angle annular dark field (HAADF)-STEM image of a $(Dy_xBi_{1-x})_2Te_3$ film with $x = 0.113$. It was acquired at 60 kV. In the image, the characteristic quintuple layer stack structure and van der Waals gap are clearly visible. In order to determine the locations of the Dy dopant in the lattice, energy-dispersive x-ray (EDX) line scans were acquired. To capture all relevant locations, the scan stretches across quintuple layer stacks and the van der Waals gap, as indicated by the orange arrow in Fig. 5(a).

Table 1 Growth parameters (effusion cell temperatures), stoichiometry (from RBS/PIXE), and structural parameters (c-axis parameter from XRD) of $(RE_xBi_{1-x})_2Te_3$ thin films [26,46,62].

RE ion	effusion cell T (°C)	RE conc. x	c (Å)
Dy	850	0.055	30.51
	875	0.113	30.52
	925	0.355	30.80
Ho	850	0.14	30.63
	865	0.21	30.73
Gd	1280	0.12	30.62
	1320	0.16	30.71
	1360	0.30	30.94
undoped	-	0	30.42

The x-ray emission intensities along the (orange) line scan are shown in Fig. 5(b). The structure of the Dy signal, which is aligned with the Bi positions and which has no intensity at the positions of the van der Waals gap, indicates that Dy is substitutionally doping on Bi sites. Furthermore, both the HAADF-STEM and EDX investigations show no evidence for clustering of the dopants or phase segregation on a local scale, in agreement with the XRD data.

3 Magnetic properties The magnetic properties of the RE doped thin film samples were studied using lab-based magnetometry for the bulk properties and synchrotron-based x-ray magnetic circular dichroism (XMCD) for determining the electronic character of the magnetic ground state [67]. Element-specific XMCD is capable of unambiguously determining the electronic and magnetic state of transition metal and rare earth magnetic dopants in TIs [68–70].

The XMCD measurements were carried out on beamline I10 (BLADE) at the Diamond Light Source (Oxfordshire, UK) using a 14 T superconducting magnet. The XMCD at the $M_{4,5}$ edges of Dy, Ho, and Gd was obtained from the difference between two x-ray absorption spectra (XAS) recorded with the x-ray helicity vector and applied magnetic field anti-parallel and parallel (along the x-ray beam), respectively [71], As changing the magnetic field of the superconducting magnet is a slow process, the XMCD was obtained by reversing the polarization of the incident x-rays. The $4f$ magnetic moments were obtained from the XMCD spectra for Dy, Ho, and Gd, as described in Refs. [26], [62], and [46], respectively, and are summarized in Table 2 along with the theoretical values for the LS-coupled atomic ground states. Table 2 shows that saturated moments obtained by XMCD at high field and near liquid He temperatures are 40-50% of the theoretical maximum values. Possible causes for this difference are an

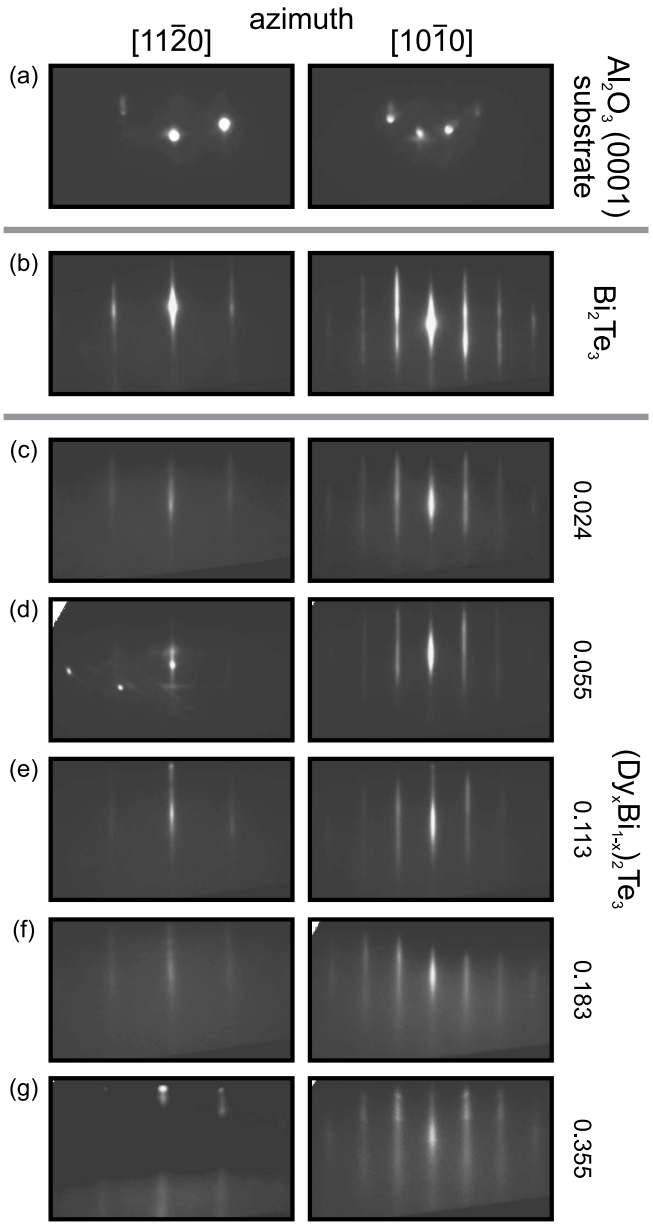

Figure 2 *In-situ* study of the growth of Dy doped Bi_2Te_3 films by reflection high energy electron diffraction (RHEED). (a) RHEED patterns along the [11$\bar{2}$0] (left column) and [10$\bar{1}$0] (right column) azimuths of the Al_2O_3(0001) (c-plane sapphire) substrate, and (b) for an undoped Bi_2Te_3 film. In (c-g), RHEED patterns are shown for a Dy thin film doping series with the (substitutional) Dy concentration x [in $(Dy_xBi_{1-x})_2Te_3$] as indicated. Up to (and including) a Dy concentration of 0.113, the streaks remain very sharp.

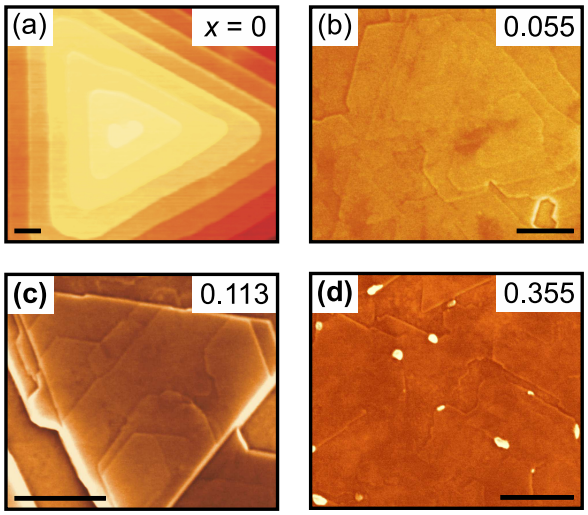

Figure 3 Microscopy images of Dy doped Bi_2Te_3 films. (a) Undoped Bi_2Te_3 film (for comparison) showing triangular terraces with quintuple layer (QL) steps of $\sim$1 nm in height. The width of the terraces is on the order of 150 nm. (b) With increasing Dy concentration ($x = 0.055$), the structures becomes more irregular, however, the QL steps are still dominant. (c) For $x = 0.113$, a moderate change in growth mode becomes apparent, whereby steps of several QL in height appear. (d) For the highest doping concentration ($x = 0.355$), the film appears much smoother with only a few steps visible, however, at the same time 3D defects appear. As a result of the 3D features, the overall roughness increases, consistent with the RHEED data. The scale bars represent 200 nm.

antiferromagnetic alignment of the oxidized RE-ions, $4f$ crystal-field interaction, and non-collinear moments in the paramagnetic phase. Note that the temperature-dependent XMCD plots reveal paramagnetic behavior down to the lowest probed temperature of $\sim$2 K.

The bulk properties of the RE doped TIs were investigated using superconducting quantum interference device (SQUID) magnetometry. Figure 6 shows $M(H)$ magnetization loops for selected Dy, Ho, and Gd concentrations. The measurements were conducted at the base temperature of the SQUID system. The field was applied in the plane, i.e., perpendicular to the c-axis. The diamagnetic background was subtracted by a linear fit to the high-field data points. For low temperatures, all magnetization curves saturate at high fields. To determine the magnetic moment per RE ion, the sample volume was calculated from the film area (via the sample mass, density, and measured wafer thickness) and film thickness (independently obtained via XRR and RBS/PIXE), and the RE concentration from RBS/PIXE [26]. The behavior of the $M(H)$ loops is qualitatively identical for all three dopants, bearing in mind that the RE concentration and measurement temperature were different for Gd. No hysteretic magnetic behavior and no apparent remanent magnetization was ob-

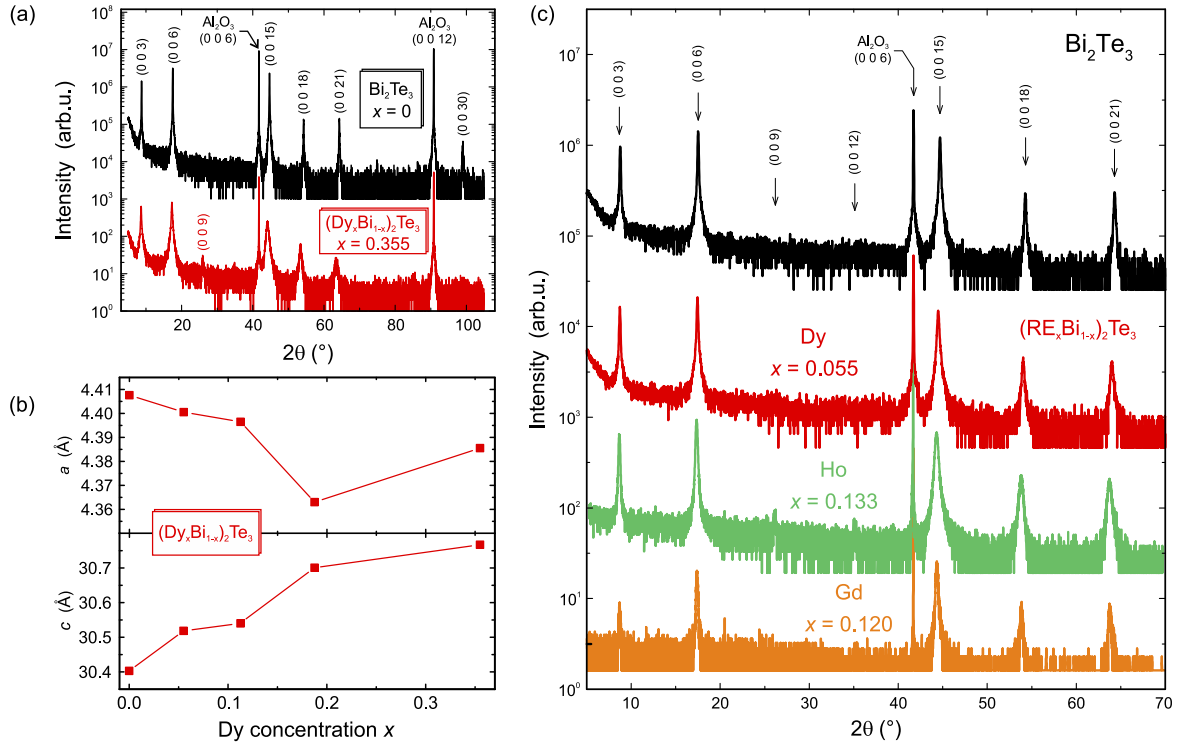

Figure 4 Structural x-ray diffraction (XRD) study of RE doped thin films. (a,b) Dy-doping series. In (a), the symmetric 2θ–ω scan of a $(Dy_xBi_{1-x})_2Te_3$ thin film with the highest doping concentration ($x = 0.355$, red) is compared with an undoped Bi_2Te_3 layer (black). The plots are offset for clarity. All film and substrate peaks are labeled as indicated. As can be seen from the peak shift, the c-axis lattice constant increases with x. In (b), the in-plane a and out-of-plane c lattice constants are plotted as a function of doping concentration, which were obtained from the analysis of the $(\bar{1}\,0\,20)$ peak in reciprocal space maps (not shown here; see Ref. [27] for details). The general trend is a decrease of a and an increase of c with x. In (c), XRD spectra for Dy, Ho, and Gd doped films (with low doping concentrations) are compared. The spectra are very similar across the entire RE series, with a larger peak shift for Ho and Gd, and a slightly lesser one for Dy. Again, an undoped Bi_2Te_3 film is shown for reference.

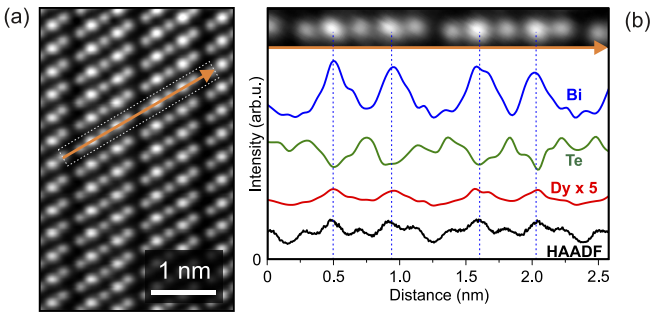

Figure 5 Electron microscopy of a $(Dy_{0.113}Bi_{0.887})_2Te_3$ thin film. (a) Cross-sectional high-angle annular dark field scanning transmission electron microscopy (HAADF-STEM) image showing quintuple layer rows, separated by the van der Waals gap. The position of the energy-dispersive x-ray (EDX) line scan is indicated by an orange arrow. (b) The scan across three van der Waals gaps shows Bi (Bi-M in blue) and Te (Te-L in green) x-ray emission intensities at their expected lateral positions in the quintuple layer, and no signal across the gaps. Equally, no Dy is detectable in the gap, but at the Bi positions, consistent with a predominantly substitutional doping scenario. Figure reproduced from CC-BY 4.0 open access publication [27].

served for any of the RE dopants at any of the investigated concentrations (at which the film quality is not compromised), consistent with the absence of long-range ferromagnetic order. The behavior for applied out-of-plane fields, i.e., parallel to the c-axis, shows a very similar (paramagnetic) response for all three dopants. This paramagnetic behavior, which is characteristic of the entire RE doping series, is due to the strongly localized character of the $4f$ electrons. As a consequence, the wave function overlap between neighboring ions is small leading to very weak or even completely suppressed interactions, as typical for the Dy-Te compounds DyTe, Dy_3Te_4, Dy_4Te_7, Dy_4Te_9, and Dy_4Te_{11} [73]. Dy_2Te_3 is an exception in that it shows antiferromagnetic ordering with a Néel temperature of 4.1 K [74].

Table 2 The spin, orbital, and total angular momenta, S, L, J, for the LS-coupled $4f$ ground state (GS) of the REs, with their corresponding effective magnetic $4f$ moment, $\mu_{\rm eff}^{\rm GS} = g_J\sqrt{J(J+1)}$ (in $\mu_{\rm B}$), using the Landé splitting factor, $g_J = 3/2 + [S(S+1) - L(L+1)]/[2J(J+1)]$. Further shown are the experimental values, $\mu_{\rm eff}^{\rm XMCD}$, obtained by XMCD for given RE concentration x, in an applied out-of-plane field $\mu_0 H$, at temperature T (see Refs. [26,62,46]). Table taken from Ref. [72].

RE ion	electron. config.	S	L	J	$\mu_{\rm eff}^{\rm GS}$ [$\mu_{\rm B}$]	$\mu_{\rm eff}^{\rm XMCD}$ [$\mu_{\rm B}$/RE ion]	x	$\mu_0 H$ [T]	T [K]	Ref.
Dy^{3+}	$4f^9$	5/2	5	15/2	10.65	4.20	0.113	7	5	[26]
Ho^{3+}	$4f^{10}$	2	6	8	10.6	4.50	0.14	7	2.5	[62]
Gd^{3+}	$4f^7$	7/2	0	7/2	7.93	4.04	0.30	6	<5	[46]

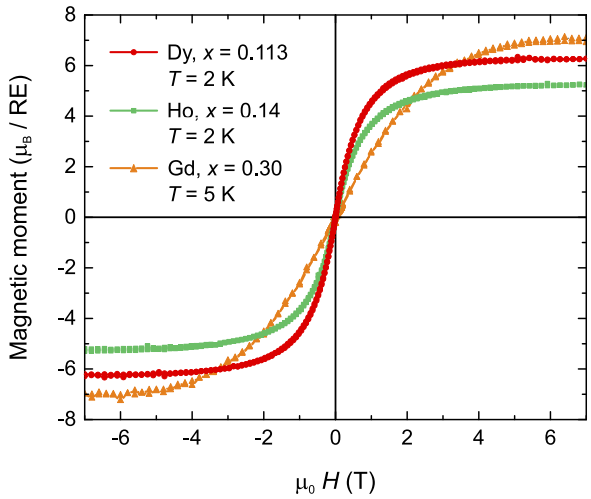

Figure 6 Comparative magnetization measurements using superconducting quantum interference device (SQUID) magnetometry. $M(H)$ loops for selected Dy and Ho doped films at 2 K, and a Gd doped film at 5 K. The field was applied in-plane. All three loops show qualitatively the same behavior, no remanent magnetization and no loop opening, indicative of the absence of ferromagnetic long-range ordering.

Figure 7 compares the temperature dependence of the magnetic susceptibility χ for the selected RE concentrations, measured in an applied magnetic field of 100 mT. The main plot shows $\chi(T)$ for a Dy doped film ($x = 0.113$), which is representative for all three dopants. The inset compares the inverse magnetic susceptibilities, $1/\chi$, as a function of temperature. The inverse magnetic susceptibility data can be fitted using the Curie-Weiss dependence $\chi = C/(T - \Theta)$ (dotted lines), where C is the material-specific Curie constant and Θ is the Weiss temperature. At low temperatures, the behavior is linear. Fitting the Curie-Weiss dependence to the Dy data ($x = 0.113$) yields a negative Weiss temperature of $\Theta = -1.2$ K. This negative value hints towards a possible antiferromagnetic phase transition at temperatures below the explored 2 K. A similar behavior was observed for all Dy doped, as well as the Ho and Gd doped layers. Note that the slope of $1/\chi$ reduces for the Dy doping series with increasing x. The Weiss temperature for Dy remains roughly x-independent with values between -0.36 K and -1.2 K, Ho gives a Θ of -0.837 K [62], and Gd of -2.5 K [46].

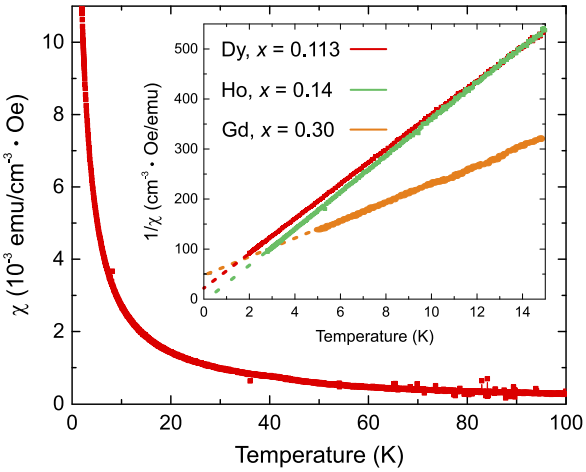

Figure 7 Temperature dependence of the magnetization. The plot shows the zero-field-cooled magnetic susceptibility χ for a Dy doped film with a doping concentration of $x = 0.113$ in a temperature range from 2 to 100 K. In the inset, a comparison of the inverse magnetic susceptibility for the three selected Dy, Ho, and Gd doped films is shown at low temperatures from 2 to 15 K. The straight lines represent linear Curie-Weiss fits to the experimental data, all yielding (small) negative Weiss temperatures.

Figure 8 shows the comparison of the magnetic moments for the Dy, Ho, and Gd doped TI films as a function of RE concentration. Interestingly, only the Dy series shows a dependence of the magnetic moment on doping concentration, whereas Ho and Gd give constant values of $\sim$5.15 $\mu_{\rm B}$/Ho [62] and $\sim$7.00 $\mu_{\rm B}$/Gd [46], respectively. The value for Gd of 7 $\mu_{\rm B}$ per $Gd3^{3+}$ ion is at the Hund's rules limit [75], i.e., Gd^{3+} is in the high-spin state. Thus, the magnetic moment observed in Gd doped Bi_2Te_3 is more than double that of Cr (in Bi_2Te_3) [5], yet Gd remains isoelectronic to Bi^{3+} whereas Cr is 2+. The value for Ho, on the other hand, is much reduced from the Hund's rules value of $\sim$10.6 $\mu_{\rm B}$/ (for Ho^{3+}) [75]. Possible reasons for this difference in moments could be oxidation of the Ho ions [72], the effects of crystal fields, as well as (par-

tial) antiferromagnetic coupling between the Ho ions [64, 76,77].

In contrast, the magnetic moment of the Dy doped films is doping concentration dependent, reaching from $(12.63 \pm 0.64)\ \mu_B$/Dy for the lowest doped sample ($x = 0.023$) to $(4.29 \pm 0.16)\ \mu_B$/Dy for the highest doped sample ($x = 0.355$), compared to the free ion magnetic moment of $10.65\ \mu_B$ [75].

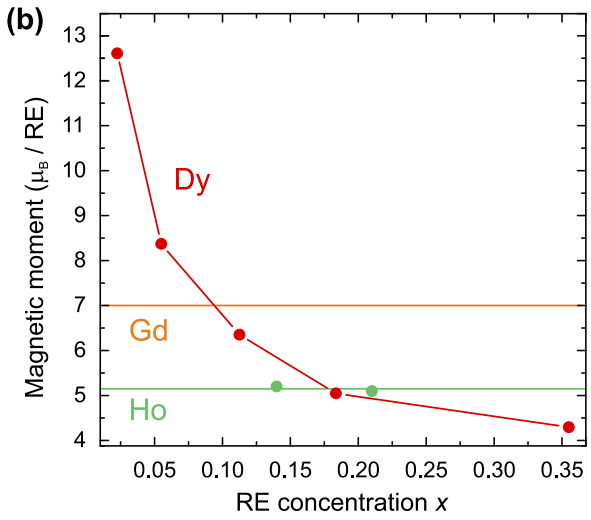

Figure 8 Comparison of the magnetic moment per RE ion as function of RE concentration (at base temperature). For the Dy doped films, a surprising concentration dependence of the effective magnetic moment $\mu_{\rm eff}$ was found, decreasing from 12.6 μ_B/Dy to 4.29 μ_B/Dy with x. In contrast, the Gd doped films show an x-independent value of $\sim$7.0 μ_B/Gd, which is close to the full Hund's rules moment, whereas the Ho doped samples show a reduced value of $\sim$5.1 μ_B/Ho.

The concentration dependence of the magnetic moment in the Dy doping series is rather unexpected. It points towards complex and competing interactions, possibly by indirect exchange or Ruderman-Kittel-Kasuya-Yosida (RKKY) interaction via the conduction electrons, as it is commonly observed for rare earth elements [75]. For Dy concentrations of $x \geq 0.055$, the effective magnetic moments are less than the Hund's rules value. This lack of moment could be due to antiferromagnetic order for the higher doped Dy samples [64,74,76,77]. In contrast, crystal-field effects and other mechanisms based on differences between surface and bulk properties are highly unlikely to be the culprit since one would not expect to find such a strong and clear concentration dependence. However, a similar behavior has also been reported for $3d$ transition metal doped TIs, i.e., this is not a RE specific phenomenon [64]. On the other end of the spectrum, low-doped Dy samples ($x < 0.055$) show magnetic moments that are considerably larger than the Hund's rule value. A possible scenario could be the spin polarization of the Bi_2Te_3 matrix by the Dy ions, which gives additional contributions to the moment. In general, such a behavior, i.e., giant magnetic moments exceeding the free ion Hund's rules value, has been observed in rare earth doped dilute magnetic semiconductors, such as Eu doped GaN [78] and Gd doped GaN [79], and has been explained by polarization of the host crystal.

4 Electronic properties The electronic properties of the RE doped thin films were studied using angle-resolved photoemission spectroscopy (ARPES). The electronic band structure of TIs is characterized by Dirac cones. A strong spectral intensity at the crossover point (Dirac point), which is found for conventional TIs, is manifestation of Kramer's degeneracy and indicates the presence of TRS in the system. If the TI is doped or otherwise perturbed with non-magnetic dopants, the TSS band remains two-fold spin-degenerate at the Dirac point, meaning that time-reversal symmetry is preserved [32]. If, however, a gap is present around the Dirac point and the TSS band dispersion becomes discontinuous, evidenced in the ARPES data by a strong reduction of spectral intensity at the Dirac point, TRS is broken [32]. Within the RE doping series, only certain Dy doped samples show a gap opening, while the Ho and Gd doped sample, albeit having almost identical structural and magnetic properties, show no gap [46, 63,80]. In the following, there review will therefore focus on Dy doped films.

Figure 9 shows ARPES data of a low and a high doping concentration Dy sample, obtained at beamline 10.0.1 of the Advanced Light Source (ALS) at Lawrence Berkeley National Laboratory. Details of the experimental setup and measurement procedure can be found in Ref. [27]. For obtaining an unoxidized surface, the thin film samples were cleaved *in situ* as outlined in Ref. [81]. The band structure was measured along the Γ-K direction. For the low doped sample ($x = 0.055$), 'V'-shaped surface states with linear dispersions are found [Fig. 9(a)], similar to the TSS in the TRS-protected, undoped Bi_2Te_3. At the Dirac point, strong spectral intensities indicate a continuous TSS band, and thus the preservation of TRS. In contrast, for the higher doped sample ($x = 0.113$) shown in Fig. 9(b), the 'V'-shaped TSS band dispersion is interrupted in the vicinity of the Dirac point and a reduced spectral intensity is found.

To further study the reduced spectral intensity near the Dirac point, energy distribution curves (EDCs) at $k_{\parallel} = 0$ were extracted. These are shown right next to the measured band structures on the right-hand side of Fig. 9(a-d). Whereas the low doped sample shows a single-peak structure of the EDC [Fig. 9(a)], and thus a continuous TSS band, the higher doped sample [Fig. 9(b)] shows a dipped, split-peak structure around the Dirac point. This dipped feature is indicative of the TSS band structure being gapped [32,82]. From the data, the size of the gap was estimated to be $\sim$85 meV. Note that the discussion so far was for data obtained at 20 K. In Figure 9(c,d), correspond-

ing plots obtained at 300 K are shown. Interestingly, the gapped structure seen for the higher doped sample stays intact. It is important to remember that the Dy doped films show no long-range ferromagnetic order at both temperatures and independent of doping concentration.

In fact, a gap in the TSS was also observed for magnetically doped TIs in the absence of long-range ferromagnetic, i.e., above the magnetic transition temperature [83]. Instead, short-range ferromagnetic order induced by inhomogeneous magnetic doping and the formation of Cr clusters has been held responsible for the gapped TSS band in ARPES measurements on $Bi_{2-x}Cr_xSe_3$ thin films [84]. An obvious culprit is impurity scattering [85,86], which has also been discussed in the context of the huge discrepancy between the calculated and observed gaps in Mn doped Bi_2Te_3 and Bi_2Se_3 — observable at temperatures well above T_C [82,87].

In the context of RE doping, however, disorder is a very unlikely sole source of the observed gap. First, it is only observed in Dy doped films, and not in the structurally and magnetically almost identical Ho and Gd doped films [46, 63,80]. Second, the doping concentration above which the gap is observed is still rather low. The structural properties of the higher doped film ($x = 0.113$ versus 0.055) are almost indistinguishable and no signs of secondary phases are visible. Currently, the question remains unanswered as the calculation of systems with highly correlated, atomic-like $4f$ electrons remains challenging [33].

5 Proximity coupling and heterostructures In order to overcome the lack of order in RE doped TIs, proximity coupling to a ferromagnet can be exploited, following the successful examples of Cr and V doped TIs in proximity to ferromagnetic insulators [88] and elemental ferromagnets [89]. Even more suited than ferromagnetic insulators, however, are other MTIs with higher transition temperatures, such as Cr doped Sb_2Te_3, with T_C's of 125 K for $x = 0.42$ [90] and 190 K for $x = 0.59$, which is approximately linearly increasing with Cr doping [91]. This combination of TIs in the form of Bi_2Te_3/Sb_2Te_3 heterostructures preserves the TSS and simplifies the growth greatly due to the similar structural properties, effectively generating a hybrid TI system with higher order temperature and high magnetic moments [92–94].

The $(Dy,Bi)_2Te_3$/$(Cr,Sb)_2Te_3$ heterostructures were grown following the same basic recipe as described above [19,26,51,70,90]. Most of results presented below were obtained on a 10 bilayer repeat sample, in which the Dy doped Bi_2Te_3 and Cr doped Sb_2Te_3 layers each were 4 nm thick. Figure 10(a,b) shows RHEED data at 2 and 5 repeats which confirm the that the growth is consistent across the stack with smooth surfaces. As before, the streaky RHEED pattern repeats every 60° revealing the symmetry of the Bi_2Te_3 and Sb_2Te_3 films (space group $R\bar{3}m$) [26,90]. Figure 10(c,d) show XRD and x-ray reflectometry (XRR) measurement data taken on an MTI heterostructure, respectively. In the 2θ-ω scan [Fig. 10(c)], only the (0 0 $3l$) family of Bi_2Te_3-related film peaks, as well as substrate peaks, can be found (as indexed). The inset shows a high-resolution 2θ-ω scan around the (0 0 15) peak, which is dominated by pronounced Kiessig fringes due to the well-ordered superlattice with well-defined interfaces. From the peak positions, a bilayer thickness of 8 nm can be extracted. The film peak positions shift in opposite directions for the Cr and Dy doped films, consistent with the substitutional incorporation on Bi sites of a larger ion in case of Dy doping [26], and a smaller one in case of Cr doping [90]. From the XRR data shown in Fig. 10(d), $(Cr,Sb)_2Te_3$ and $(Dy,Bi)_2Te_3$ thicknesses of 3.5 nm and 3.8 nm, respectively, with roughnesses of around 1 nm were extracted using 10-bilayer repeat model (red curve, simulation).

To determine the T_C's of the Dy and Cr doped layers separately, the magnetization is measured element-selectively by XMCD as a function of applied magnetic field (H) and temperature. The magnetization M is proportional to the XMCD peak asymmetry at the Cr L_3 and Dy M_5 edges, respectively [89]. The most reliable way to determine T_C is via the Arrott criterion [96], which suppresses contributions from multidomain states and magnetic anisotropies to the apparent T_C in a simple $M(T)$ plot. An Arrott plot is a set of temperature-dependent plots of M^2 vs. H/M, which are linear at higher magnetic fields. At lower applied fields, the isotherms are not necessarily linear, e.g., due to disorder in the system [97]. For the Cr layers, parallel straight lines can be fitted to the respective high field data points (see Ref. [95]). T_C is then defined as the temperature at which $M^2 = 0$, i.e., the H/M intercept values are positive for $T > T_C$ and negative for $T < T_C$. Figure 11(a) shows a plot of $H/M(T)$ intercept values for Cr, from which $T_C \approx 70$ K is obtained. This T_C is in good agreement with the values typical for similarly doped $(Cr,Sb)_2Te_3$ single layers [90]. In contrast, the Dy plots can not be fitted with linear fits of a fixed slope across the entire temperature region. This behavior is common for magnetically disordered systems [97]. In this case, linear fits with a common slope are fitted separately for $T > T_C$ and $T < T_C$, and the plot of the intercepts is shown in Fig. 11(b). For this plot, a Dy T_C of $\sim$17 K is found, i.e., the sandwiched layer is ferromagnetically ordered resulting from the proximity coupling to $(Cr,Sb)_2Te_3$.

A deeper understanding of the coupling between different magnetic layers can be achieved by carrying out theoretical calculations [95]. A successful recent example of combined theoretical and experimental work are MTI-antiferromagnet heterostructures in which interfacial spin textures were obtained via enhanced proximity coupling [88,89,98,99]. The magnetic interaction in an isolated Cr doped Sb_2Te_3 film is predominantly positive, i.e., the coupling between the Cr moments is ferromagnetic and relatively strong with an ordering temperature of 102 K. For comparison, the experimentally determined T_C is 70 K. On

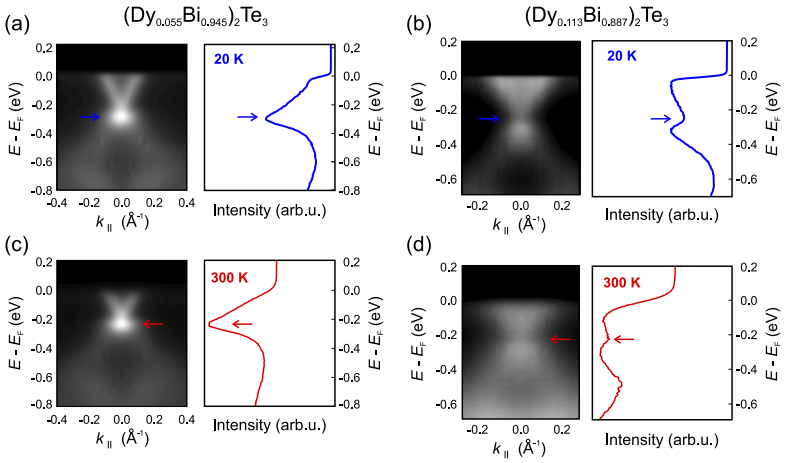

Figure 9 Angle-resolved photoemission spectroscopy (ARPES) results for Dy doped films with with low and high doping concentration. (a,c) Band structures along the K–Γ–K direction and energy distribution curves along $k_{\|}$=0 for the low-doped ($x = 0.055$) sample. (b,d) Corresponding plots for the $x = 0.113$ sample. The measurements were carried out at base temperature (20 K) and room temperature (300 K) as shown in the top and bottom row, respectively. The relative locations of the Dirac points in the band structure and energy distribution curves are indicated by arrows. Whereas for the low-doped sample, a strong spectral intensity is found at the Dirac point at both temperatures, the higher doped sample shows a ∼85 meV wide gap, which persists up to room temperature. Figure reproduced from CC-BY 4.0 open access publication [27].

the other hand, in an isolated layer of Dy doped Bi_2Te_3, the paramagnetic behavior can be ascribed to the almost equal population of the two spin channels. Nevertheless, within a (Bi) layer, there exists a strong, ferromagnetic exchange interaction between the Dy moments with a T_C of 5 K, while the intralayer coupling is very small resulting in an overall frustrated magnetic system.

When $(Cr,Sb)_2Te_3$ and $(Dy,Bi)_2Te_3$ are coupled together, sharing a common interface, the hole in the majority spin channel of Cr doped Sb_2Te_3 polarizes the hole in the Dy doped Bi_2Te_3 layer, leading to an enhanced magnetic interaction. Furthermore, the number of (almost) free electrons in the Dy layer is increased due to the proximity to the Cr layer. These electrons then mediate a stronger indirect exchange interaction via the RKKY mechanism, which means that the Dy films become long-range ferromagnetically ordered. Note that the thicknesses of the layers in the stack can be reduced to a point where the magnetic coupling is predominantly mediated by the TSS electrons [100]. The theoretical estimated for the Dy T_C is 23 K close to the interface, in good agreement with the experimentally determined value in the thin-layer superlattice.

In the future, ARPES and transport measurements will be carried out on the $(Dy,Bi)_2Te_3/(Cr,Sb)_2Te_3$ heterostructures to study their electronic properties as a function of the individual film thicknesses and number of repeats. In particular, the resistivities of the layers have to be carefully adjusted to assure that transport is dominated by the layer of choice. Finally, in order to further optimize the structural quality of the layer stacks, TEM will be employed. This is particular important in order to rule out the diffusion of the respective transition metal and rare earth dopants across the interfaces, as the character of these dopants is largely different.

6 Summary and conclusions In summary, the structural, electronic, and magnetic properties of RE doped Bi_2Te_3 TI thin films grown by MBE have been reviewed. In contrast to doped bulk crystals, Dy, Ho, and Gd can be substitutionally incorporated into the host lattice on Bi sites up to large concentrations, maintaining the rhombohedral crystal structure of Bi_2Te_3, and without forming secondary phases. In Gd doped films, the full magnetic moment of 7.0 μ_B/RE ion was achieved, whereas the effective moment in Ho doped films was about half the theoretical value. For the Dy doped films, the effective magnetic moment is decreasing with doping concentration. The high moments seen for low Dy concentrations ($x \leq 0.023$) indicates the possibility of the polarization of the Bi_2Te_3 host crystal, i.e., the magnetic doping mechanism is fundamentally different from the Ho and Gd doped films. Nevertheless, all films show paramagnetic behavior from bulk-sensitive SQUID magnetization measurements, with some hints of possible antiferromagnetic order below ∼2 K. Measurements of the electronic bandstructure show that the TSS remains gapless upon Ho and Gd doping. In contrast, Dy doped films above a certain doping concentration show a gap in the TSS, which remains intact at room temperature. This gap is existing despite the absence of long-range magnetic order in the Dy doped films.

Despite the fact that a thin film of Dy doped Bi_2Te_3 on its own is paramagnetic, calculations have shown that the exchange interaction between Dy moments is leading to ferromagnetic order within a Dy doped Bi layer, however, there is no coupling between Dy doped layers. This scenario of an almost-ordered system can be exploited in heterostructures making use of the proximity effect. In combination with Cr doped Sb_2Te_3, which is strongly ferromagnetically ordered up to above 150 K, MBE-grown $(Cr,Sb)_2Te_3/(Dy,Bi)_2Te_3$ heterostructures of high crystalline quality and with well-defined interfaces have been demonstrated. In these, Dy doped Bi_2Te_3 films exhibit ferromagnetic ordering up to ∼17 K, which has been unambiguously confirmed using XMCD. Proximity coupling across interfaces, and multiplied in superlattices, is a ver-

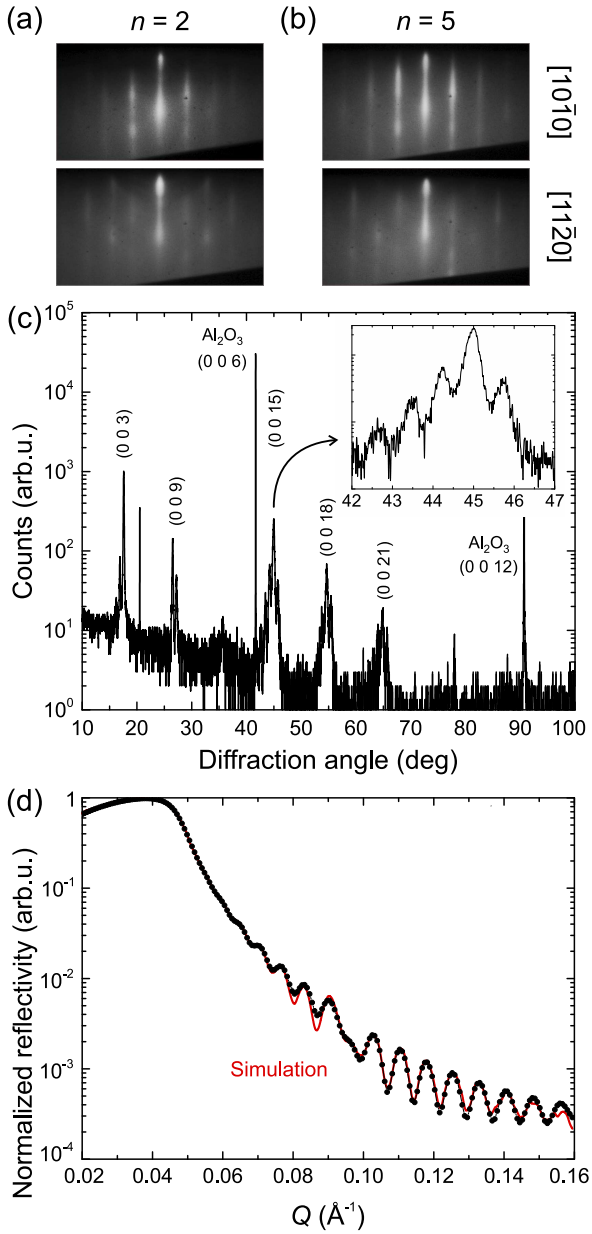

Figure 10 Study of the structural properties of $(Dy_xBi_{1-x})_2Te_3$/$(Cr_xSb_{1-x})_2Te_3$ superlattice samples. (a) RHEED patterns of the Cr doped Sb_2Te_3 surface after (a) $n = 2$ and (b) $n = 5$ bilayer repeats, obtained along the $[10\bar{1}0]$ and $[11\bar{2}0]$ azimuths. (c) 2θ-ω XRD spectrum of the superlattice. The inset highlights superlattice peaks around the $(0\,0\,15)$ Bragg peak of the film. (d) X-ray reflectometry (XRR) scan as a function of momentum transfer Q showing the experimental data in black and the simulation in red. Adapted with permission [95]. Copyright (2018) by the American Physical Society.

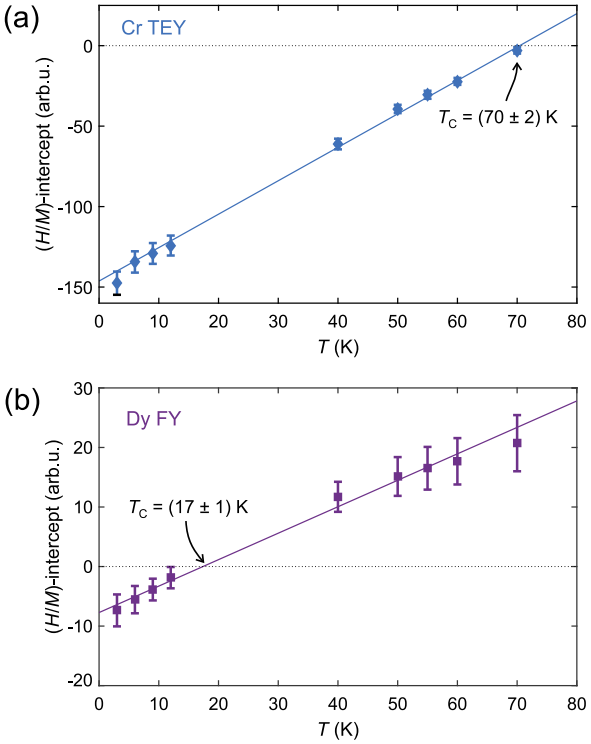

Figure 11 Extraction of the magnetic transition temperatures of the Cr and Dy doped layers using the Arrott plot analysis of the XMCD hysteresis loops. First, M^2 vs H/M Arrott plots (magnetization M, field H) have to be obtained from the Cr L_3 and Dy M_5 loops (for details, see Ref. [95]). From linear fits to the high-field data, H/M-intercepts are obtained, which are plotted as a function of temperature for Cr (a) and Dy (b). From fits to these data points, a T_C of 70 K is obtained for the Cr doped layer and of 17 K for the Dy doped layer. This dramatic increase in the T_C of Dy doped Bi_2Te_3 illustrates that the proximity effect in heterostructures can be used to imprint long-range magnetic order from the Cr doped layer onto the the high moment rare earth doped layer. Reprinted figure panels with permission [95]. Copyright (2018) by the American Physical Society.

satile principle that opens the door for above liquid helium temperature studies of novel quantum phenomena in TIs.

Acknowledgements I am indebted to all my colleagues and collaborators who co-authored the work I was reviewing here, and in particular the former graduate student Dr. Sarah E. Harrison for her groundbreaking contributions to the field of RE doping. I further thank the group alumni Drs. Liam B. Duffy, Piet Schönherr, Alexander A. Baker, and Liam J. Collins-McIntyre, as well as Prof. Yulin Chen from Oxford University, Dr. Vesna Srot and Prof. Peter A. van Aken from the MPI Stuttgart, Dr. Aakash Pushp and Prof. Stuart S. P. Parkin from IBM Almaden, Prof. James S. Harris from Stanford University, Dr. Nina J. Steinke and Prof. Sean Langridge from ISIS/STFC, and

last but not least Dr. Adriana I. Figueroa and Prof. Gerrit van der Laan from Diamond Light Source. This work was primarily supported by the John Fell Oxford University Press (OUP) Research Fund, as well as the European Union Seventh Framework Programme (Grant Agreement 312483; ESTEEM2, Integrated Infrastructure Initiative I3), DARPA MESO (project No. N66001-11-1-4105) and the Army Research Laboratories. The Research Complex at Harwell (RCaH) is gratefully acknowledged for their hospitality. The graduate students were supported by scholarships from EPSRC (L.C.M., L.B.D., P.S.), ISIS/STFC (L.B.D.), the Studienstiftung des deutschen Volkes (P.S.), the Department of Defense and the VPGE of Stanford University (S.E.H.). Diamond Light Source, the ESRF, ALBA, ILL, and ISIS/STFC are acknowledged for awarding many successful beamtimes.

Thorsten Hesjedal is a Professor of Condensed Matter Physics at the University of Oxford, working on quantum materials in the form of thin films and nanostructures. He graduated with a Dr. rer. nat. in physics from the Humboldt University in Berlin, Germany. He held a faculty position at the University of Waterloo (Canada), and visiting faculty positions at Stanford University and UC Santa Barbara. At the Clarendon Laboratory and the Rutherford Appleton Laboratory, he operates several molecular beam epitaxy, physical and chemical vapor deposition systems for the synthesis of a wide range of advanced magnetic and electronic materials. He has published more than 190 papers in the field.

References

[1] C. Kane and E. Mele, Phys. Rev. Lett. **95**, 146802 (2005).
[2] B. A. Bernevig and S. C. Zhang, Phys. Rev. Lett. **96**, 106802 (2006).
[3] H. Zhang and S. C. Zhang, Phys. Status Solidi RRL **7**, 72–81 (2013).
[4] L. Fu and C. L. Kane, Phys. Rev. Lett. **100**, 096407 (2008).
[5] C. Z. Chang, J. Zhang, X. Feng, J. Shen, Z. Zhang, M. Guo, K. Li, Y. Ou, P. Wei, L. L. Wang, Z. Q. Ji, Y. Feng, S. Ji, X. Chen, J. Jia, X. Dai, Z. Fang, S. C. Zhang, K. He, Y. Wang, L. Lu, X. C. Ma, and Q. K. Xue, Science **340**, 167–170 (2013).
[6] X. L. Qi, T. L. Hughes, S. Raghu, and S. C. Zhang, Phys. Rev. Lett. **102**, 187001 (2009).
[7] D. Pesin and A. H. MacDonald, Nat. Mater. **11**, 409–416 (2012).
[8] C. Niu, Y. Dai, M. Guo, W. Wei, Y. Ma, and B. Huang, Appl. Phys. Lett. **98**, 252502 (2011).
[9] C. Z. Chang, K. He, L. L. Wang, X. C. Ma, M. H. Liu, Z. C. Zhang, X. Chen, Y. Y. Wang, and Q. K. Xue, SPIN **1**, 21–25 (2011).
[10] V. Kulbachinskii, A. Y. Kaminskii, K. Kindo, Y. Narumi, K. Suga, P. Lostak, and P. Svanda, Physica B **311**, 292–297 (2002).
[11] J. Choi, S. Choi, J. Choi, Y. Park, H. Park, H. Lee, B. Woo, and S. Cho, Phys. Status Solidi B **241**, 1541–1544 (2004).
[12] J. W. G. Bos, M. Lee, E. Morosan, H. W. Zandbergen, W. L. Lee, N. P. Ong, and R. J. Cava, Phys. Rev. B **74**, 184429 (2006).
[13] Y. S. Hor, P. Roushan, H. Beidenkopf, J. Seo, D. Qu, J. G. Checkelsky, L. A. Wray, D. Hsieh, Y. Xia, S. Y. Xu, D. Qian, M. Z. Hasan, N. P. Ong, A. Yazdani, and R. J. Cava, Phys. Rev. B **81**, 195203 (2010).
[14] J. Dyck, v. Drašar, P. Lošťák, and C. Uher, Phys. Rev. B **71**, 115214 (2005).
[15] C. Z. Chang, J. Zhang, M. Liu, Z. Zhang, X. Feng, K. Li, L. L. Wang, X. Chen, X. Dai, Z. Fang, X. L. Qi, S. C. Zhang, Y. Wang, K. He, X. C. Ma, and Q. K. Xue, Adv. Mater. **25**, 1065–1070 (2013).
[16] C. Z. Chang, W. Zhao, D. Y. Kim, H. Zhang, B. A. Assaf, D. Heiman, S. C. Zhang, C. Liu, M. H. W. Chan, and J. S. Moodera, Nat. Mater. **14**, 473 (2015).
[17] Z. Zhou, Y. J. Chien, and C. Uher, Phys. Rev. B **74**, 224418 (2006).
[18] I. Lee, C. K. Kim, J. Lee, S. J. L. Billinge, R. Zhong, J. A. Schneeloch, T. Liu, T. Valla, J. M. Tranquada, G. Gu, and J. C. S. Davis, Proc. Natl. Acad. Sci. U.S.A **112**, 1316–1321 (2015).
[19] A. I. Figueroa, G. van der Laan, L. J. Collins-McIntyre, S. L. Zhang, A. A. Baker, S. E. Harrison, P. Schönherr, G. Cibin, and T. Hesjedal, Phys. Rev. B **90**, 134402 (2014).
[20] A. I. Figueroa, G. van der Laan, L. J. Collins-McIntyre, G. Cibin, A. J. Dent, and T. Hesjedal, J. Phys. Chem. C **119**, 17344 (2015).
[21] v. Drašar, J. Kašparová, P. Lošťák, X. Shi, and C. Uher, Phys. Stat. Sol. (b) **244**, 2202–2209 (2007).
[22] A. N. Andriotis and M. Menon, Phys. Rev. B **87**(Apr), 155309 (2013).
[23] Y. Ou, C. Liu, G. Jiang, Y. Feng, D. Zhao, W. Wu, X. X. Wang, W. Li, C. Song, L. L. Wang, W. Wang, W. Wu, Y. Wang, K. He, X. C. Ma, and Q. K. Xue, Adv. Mater. **30**, 1703062 (2018).
[24] X. Kou, L. He, M. Lang, Y. Fan, K. Wong, Y. Jiang, T. Nie, W. Jiang, P. Upadhyaya, Z. Xing, Y. Wang, F. Xiu, R. N. Schwartz, and K. L. Wang, Nano Lett. **13**, 4587–4593 (2013).
[25] M. Mogi, R. Yoshimi, A. Tsukazaki, K. Yasuda, Y. Kozuka, K. S. Takahashi, M. Kawasaki, and Y. Tokura, Appl. Phys. Lett. **107**, 182401 (2015).
[26] S. E. Harrison, L. J. Collins-McIntyre, S. L. Zhang, A. A. Baker, A. I. Figueroa, A. J. Kellock, A. Pushp, S. S. P. Parkin, J. S. Harris, G. van der Laan, and T. Hesjedal, J. Phys.: Condens. Matter **27**, 245602 (2015).
[27] S. E. Harrison, L. J. Collins-McIntyre, P. Schönherr, A. Vailionis, V. Srot, P. A. van Aken, A. J. Kellock, A. Pushp, S. S. P. Parkin, J. S. Harris, B. Zhou, Y. L. Chen, and T. Hesjedal, Sci. Rep. **5**, 15767 (2015).
[28] L. B. Duffy, A. I. Figueroa, G. van der Laan, and T. Hesjedal, Phys. Rev. Materials **1**, 064409 (2017).
[29] M. Mogi, M. Kawamura, R. Yoshimi, A. Tsukazaki, Y. Kozuka, N. Shirakawa, K. S. Takahashi, M. Kawasaki, and Y. Tokura, Nat. Mater. **16**, 516–521 (2017).
[30] R. Dingle, H. L. Störmer, A. C. Gossard, and W. Wiegmann, Appl. Phys. Lett. **33**, 665–667 (1978).

[31] H. L. Störmer, A. Pinczuk, A. C. Gossard, and W. Wiegmann, Appl. Phys. Lett. **38**, 691–693 (1981).
[32] Y. Chen, J. H. Chu, J. Analytis, Z. Liu, K. Igarashi, H. H. Kuo, X. Qi, S. K. Mo, R. Moore, D. Lu, M. Hashimoto, T. Sasagawa, S. C. Zhang, I. R. Fisher, Z. Hussain, and Z. X. Shen, Science **329**, 659–662 (2010).
[33] P. Söderlind, P. E. A. Turchi, A. Landa, and V. Lordi, J. Phys.: Condens. Matter **26**, 416001 (2014).
[34] C. G. Olson, S. J. Chase, P. C. Canfield, and D. W. Lynch, J. Electron Spectrosc. Relat. Phenom. **93**, 175–180 (1998).
[35] H. J. Im, T. Ito, H. D. Kim, S. Kimura, K. E. Lee, J. B. Hong, Y. S. Kwon, A. Yasui, and H. Yamagami, Phys. Rev. Lett. **100**, 176402 (2008).
[36] D. V. Vyalikh, S. Danzenbaecher, A. N. Yaresko, M. Holder, Y. Kucherenko, C. Laubschat, C. Krellner, Z. Hossain, C. Geibel, M. Shi, L. Patthey, and S. L. Molodtsov, Phys. Rev. Lett. **100**, 056402 (2008).
[37] Y. B. Losovyj, D. Wooten, J. C. Santana, J. M. An, K. D. Belashchenko, N. Lozova, J. Petrosky, A. Sokolov, J. Tang, W. D. Wang, N. Arulsamy, and P. A. Dowben, J. Phys.: Condens. Matter **21**, 045602 (2009).
[38] B. Yan, H. J. Zhang, C. X. Liu, X. L. Qi, T. Frauenheim, and S. C. Zhang, Phys. Rev. B **82**, 161108 (2010).
[39] F. Zheng, Q. Zhang, Q. Meng, B. Wang, L. Fan, L. Zhu, F. Song, and G. Wang, Chalcogenide Lett. **14**, 551–560 (2017).
[40] J. Liu and D. Vanderbilt, Phys. Rev. B **90**, 155316 (2014).
[41] M. Elkholdi, M. Averous, S. Charar, C. Fau, G. Brun, H. Ghoumaribouanani, and J. Deportes, Phys. Rev. B **49**, 1711–1715 (1994).
[42] Y. R. Song, F. Yang, M. Y. Yao, F. Zhu, L. Miao, J. P. Xu, M. X. Wang, H. Li, X. Yao, F. Ji, S. Qiao, Z. Sun, G. B. Zhang, B. Gao, C. Liu, D. Qian, C. L. Gao, and J. F. Jia, Appl. Phys. Lett. **100**, 242403 (2012).
[43] D. R. Behrendt, S. Legvold, and F. H. Spedding, Phys. Rev. **109**, 1544–1547 (1958).
[44] M. K. Wilkinson, J. W. Cable, E. O. Wollan, and W. C. Koehler, J. Appl. Phys. **32**, S48–S49 (1961).
[45] F. J. Darnell and E. P. Moore, J. Appl. Phys. **34**, 1337–1338 (1963).
[46] S. E. Harrison, L. J. Collins-McIntyre, S. Li, A. A. Baker, L. R. Shelford, Y. Huo, A. Pushp, S. S. P. Parkin, J. S. Harris, E. Arenholz, G. van der Laan, and T. Hesjedal, J. Appl. Phys. **115**, 023904 (2014).
[47] L. He, F. Xiu, Y. Wang, A. V. Fedorov, G. Huang, X. Kou, M. Lang, W. P. Beyermann, J. Zou, and K. L. Wang, J. Appl. Phys. **109**, 103702 (2011).
[48] J. Krumrain, G. Mussler, S. Borisova, T. Stoica, L. Plucinski, C. Schneider, and D. Grützmacher, J. Cryst. Growth **324**, 115–118 (2011).
[49] X. Liu, D. J. Smith, J. Fan, Y. Zhang, H. Cao, Y. P. Chen, B. J. Kirby, N. Sun, S. T. Ruggiero, J. Leiner, R. E. Pimpinella, J. Hagmann, K. Tivakornsasithorn, M. Dobrowolska, and J. K. Furdyna, AIP Conf. Proc. **1416**, 105–108 (2011).
[50] Y. Liu, M. Weinert, and L. Li, Phys. Rev. Lett. **108**, 115501 (2012).
[51] S. E. Harrison, S. Li, Y. Huo, B. Zhou, Y. L. Chen, and J. S. Harris, Appl. Phys. Lett. **102**, 171906 (2013).
[52] Y. Zhao, C. Z. Chang, Y. Jiang, A. DaSilva, Y. Sun, H. Wang, Y. Xing, Y. Wang, K. He, X. Ma, Q. K. X. Xue, and J. Wang, Sci. Rep. **3**, 3060 (2013).
[53] Z. Chen, T. A. Garcia, J. De Jesus, L. Zhao, H. Deng, J. Secor, M. Begliarbekov, L. Krusin-Elbaum, and M. C. Tamargo, J. Electron. Mater. **43**, 909–913 (2014).
[54] M. Eddrief, P. Atkinson, V. Etgens, and B. Jusserand, Nanotechnology **25**, 245701 (2014).
[55] X. Liu, D. J. Smith, J. Fan, Y. H. Zhang, H. Cao, Y. P. Chen, J. Leiner, B. J. Kirby, M. Dobrowolska, and J. K. Furdyna, Appl. Phys. Lett. **99**, 171903 (2011).
[56] S. Schreyeck, N. V. Tarakina, G. Karczewski, C. Schumacher, T. Borzenko, C. Brune, H. Buhmann, C. Gould, K. Brunner, and L. W. Molenkamp, Appl. Phys. Lett. **102**, 041914 (2013).
[57] X. Guo, Z. J. Xu, H. C. Liu, B. Zhao, X. Q. Dai, H. T. He, J. N. Wang, H. J. Liu, W. K. Ho, and M. H. Xie, Appl. Phys. Lett. **102**, 151604 (2013).
[58] S. Jerng, K. Joo, Y. Kim, S. Yoon, J. Lee, M. Kim, J. Kim, E. Yoon, S. Chun, and Y. Kim, Nanoscale **5**, 10618 (2013).
[59] N. Bansal, M. R. Cho, M. Brahlek, N. Koirala, Y. Horibe, J. Chen, W. Wu, Y. D. Park, and S. Oh, Nano Lett. **14**, 1343–1348 (2014).
[60] J. H. Jeon, M. Song, H. Kim, W. J. Jang, J. Y. Park, S. Yoon, and S. J. Kahng, Appl. Surf. Sci. **316**, 42–45 (2014).
[61] L. J. Collins-McIntyre, W. Wang, B. Zhou, S. C. Speller, Y. L. Chen, and T. Hesjedal, Phys. Status Solidi B **252**, 1334–1338 (2015).
[62] S. E. Harrison, L. J. Collins-McIntyre, S. L. Zhang, A. A. Baker, A. I. Figueroa, A. J. Kellock, A. Pushp, Y. Chen, S. S. P. Parkin, J. S. Harris, G. van der Laan, and T. Hesjedal, Appl. Phys. Lett. **107**, 182406 (2015).
[63] S. Li, S. Harrison, Y. Huo, A. Pushp, H. T. Yuan, B. Zhou, A. J. Kellock, S. S. P. Parkin, Y. L. Chen, T. Hesjedal, and J. S. Harris, Appl. Phys. Lett. **102**, 242412 (2013).
[64] P. P. J. Haazen, J. B. Laloë, T. J. Nummy, H. J. M. Swagten, P. Jarillo-Herrero, D. Heiman, and J. S. Moodera, Appl. Phys. Lett. **100**, 082404 (2012).
[65] O. Madelung, U. Rössler, and M. Schulz, Landolt-Börnstein - Group III Condensed Matter, Volume 41E (Springer, Berlin, 2000).
[66] L. J. Collins-McIntyre, M. D. Watson, A. A. Baker, S. L. Zhang, A. I. Coldea, S. E. Harrison, A. Pushp, A. J. Kellock, S. S. P. Parkin, G. van der Laan, and T. Hesjedal, AIP Adv. **4**, 127136 (2014).
[67] G. van der Laan, J. Phys.: Conf. Ser. **430**, 012127 (2013).
[68] L. R. Shelford, T. Hesjedal, L. Collins-McIntyre, S. S. Dhesi, F. Maccherozzi, and G. van der Laan, Phys. Rev. B **86**, 081304 (2012).
[69] M. D. Watson, L. J. Collins-McIntyre, L. R. Shelford, A. I. Coldea, D. Prabhakaran, S. C. Speller, T. Mousavi, C. R. M. Grovenor, Z. Salman, S. R. Giblin, G. van der Laan, and T. Hesjedal, New J. Phys. **15**, 103016 (2013).
[70] L. J. Collins-McIntyre, S. E. Harrison, P. Schönherr, N. J. Steinke, C. J. Kinane, T. R. Charlton, D. Alba-Veneroa, A. Pushp, A. J. Kellock, S. S. P. Parkin, J. S. Harris, S. Langridge, G. van der Laan, and T. Hesjedal, EPL (Europhys. Lett.) **107**, 57009 (2014).

[71] G. van der Laan and A. I. Figueroa, Coord. Chem. Rev. **277-278**, 95–129 (2014).
[72] A. I. Figueroa, G. van der Laan, S. E. Harrison, G. Cibin, and T. Hesjedal, Sci. Rep. **6**, 22935.
[73] I. Hinz, P. Kuhn, U. Vetter, E. Warkentin, H. Bergmann, and H. Hein, Gmelin Handbook of Inorganic Chemistry, Rare Earth Elements and Tellurium (Springer, Heidelberg, 1986).
[74] S. Pokrzywnicki, J. Alloys Compd. **225**, 163–165 (1995).
[75] J. Jensen and A. R. Mackintosh, Rare Earth Magnetism (Clarendon Press, Oxford, 1991).
[76] O. Zhong-Wen and R. Guang-Hui, Chin. Phys. B **22**, 097501 (2013).
[77] A. Majid, A. Dar, and J. J. Zhu, J. Magn. Magn. Mater. **374**, 676–679 (2015).
[78] V. Kachkanov, M. J. Wallace, G. van der Laan, S. S. Dhesi, S. A. Cavill, Y. Fujiwara, and K. P. O'Donnell, Sci. Rep. **2**, 969 (2012).
[79] S. Dhar, O. Brandt, M. Ramsteiner, V. F. Sapega, and K. H. Ploog, Phys. Rev. Lett. **94**, 037205 (2005).
[80] S. E. Harrison, Binary and Rare Earth-Doped Topological Insulator Thin Films, PhD thesis, Stanford University, March 2015.
[81] S. E. Harrison, B. Zhou, Y. Huo, A. Pushp, A. J. Kellock, S. S. P. Parkin, J. S. Harris, Y. Chen, and T. Hesjedal, Appl. Phys. Lett. **105**, 121608 (2014).
[82] S. Y. Xu, M. Neupane, C. Liu, D. Zhang, A. Richardella, L. A. Wray, N. Alidoust, M. Leandersson, T. Balasubramanian, J. Sanchez-Barriga, O. Rader, G. Landolt, B. Slomski, J. H. Dil, J. Osterwalder, T. R. Chang, H. T. Jeng, H. Lin, A. Bansil, N. Samarth, and M. Z. Hasan, Nature Phys. **8**, 616–622 (2012).
[83] M. Franz and L. Molenkamp, Topological Insulators, Volume 6 (Elsevier Science, 2013).
[84] C. Z. Chang, P. Tang, Y. L. Wang, X. Feng, K. Li, Z. Zhang, Y. Wang, L. L. Wang, X. Chen, C. Liu, W. Duan, K. He, X. C. Ma, and Q. K. Xue, Phys. Rev. Lett. **112**, 056801 (2014).
[85] Z. Alpichshev, R. R. Biswas, A. V. Balatsky, J. G. Analytis, J. H. Chu, I. R. Fisher, and A. Kapitulnik, Phys. Rev. Lett. **108**, 206402 (2012).
[86] A. M. Black-Schaffer and A. V. Balatsky, Phys. Rev. B **85**, 121103 (2012).
[87] J. Henk, A. Ernst, S. V. Eremeev, E. V. Chulkov, I. V. Maznichenko, and I. Mertig, Phys. Rev. Lett. **108**, 206801 (2012).
[88] M. Li, C. Z. Chang, B. J. Kirby, M. E. Jamer, W. Cui, L. Wu, P. Wei, Y. Zhu, D. Heiman, J. Li, and J. S. Moodera, Phys. Rev. Lett. **115**, 087201 (2015).
[89] A. A. Baker, A. I. Figueroa, K. Kummer, L. J. Collins-McIntyre, T. Hesjedal, and G. van der Laan, Phys. Rev. B **92**, 094420 (2015).
[90] L. J. Collins-McIntyre, L. B. Duffy, A. Singh, N. J. Steinke, C. J. Kinane, T. R. Charlton, A. Pushp, A. J. Kellock, S. S. P. Parkin, S. N. Holmes, C. H. W. Barnes, G. van der Laan, S. Langridge, and T. Hesjedal, EPL (Europhys. Lett.) **115**, 27006 (2016).
[91] Z. Zhou, Y. J. Chien, and C. Uher, Phys. Rev. B **74**, 224418 (2006).
[92] R. Venkatasubramanian, T. Colpitts, E. Watko, M. Lamvik, and N. ElMasry, J. Cryst. Growth **170**, 817 (1997).
[93] Y. Iwata, H. Kobayashi, S. Kikuchi, E. Hatta, and K. Mukasa, J. Cryst. Growth **203**, 125–130 (1999).
[94] M. Lanius, J. Kampmeier, C. Weyrich, S. Kölling, M. Schall, P. Schüffelgen, E. Neumann, M. Luysberg, G. Mussler, P. M. Koenraad, T. Schäpers, and D. Grützmacher, Cryst. Growth Des. **16**, 2057–2061 (2016).
[95] L. B. Duffy, A. Frisk, D. M. Burn, N. J. Steinke, J. Herrero-Martin, A. Ernst, G. van der Laan, and T. Hesjedal, Phys. Rev. Materials **2**, 054201 (2018).
[96] A. Arrott and J. E. Noakes, Phys. Rev. Lett. **19**, 786 (1967).
[97] I. Yeung, R. M. Roshko, and G. Williams, Phys. Rev. B **34**, 3456–3457 (1986).
[98] Q. L. He, X. Kou, A. J. Grutter, G. Yin, L. Pan, X. Che, Y. Liu, T. Nie, B. Zhang, S. M. Disseler, B. J. Kirby, W. Ratcliff II, Q. Shao, K. Murata, X. Zhu, G. Yu, Y. Fan, M. Montazeri, X. Han, J. A. Borchers, and K. L. Wang, Nat. Mater. **16**, 94–100 (2017).
[99] T. Hesjedal and Y. Chen, Nat. Mater. **16**, 3–4 (2017).
[100] P. Rüßmann, S. K. Mahatha, P. Sessi, M. A. Valbuena, T. Bathon, K. Fauth, S. Godey, A. Mugarza, K. A. Kokh, O. E. Tereshchenko, P. Gargiani, M. Valvidares, E. Jiménez, N. B. Brookes, M. Bode, G. Bihlmayer, S. Blügel, P. Mavropoulos, C. Carbone, and A. Barla, J. Phys. Mater. **1**(1), 015002 (2018).